

Available online at www.sciencedirect.com

SciVerse ScienceDirect

journal homepage: www.elsevier.com/locate/he

Numerical investigation of liquid water distribution in the cathode side of proton exchange membrane fuel cell and its effects on cell performance

Li Chen, Tao-Feng Cao, Zhao-Hui Li, Ya-Ling He, Wen-Quan Tao*

Key Laboratory of Thermo-Fluid Science & Engineering, School of Energy & Power Engineering, Xi'an Jiaotong University, No.28, Xianning West Road, Xi'an, Shannxi 710049, PR China

ARTICLE INFO

Article history:

Received 17 September 2011

Received in revised form

18 January 2012

Accepted 22 January 2012

Available online 30 March 2012

Keywords:

Proton exchange membrane fuel cell

Gas channel

Gas diffusion layer

Liquid water

Cell performance

Numerical simulation

ABSTRACT

A three-dimensional unsteady two-phase model for the cathode side of proton exchange membrane fuel cell (PEMFC) consisting of gas diffusion layer (GDL) with hybrid structural model is developed to investigate liquid water behaviors under different operating and geometrical conditions and to quantitatively evaluate effects of liquid water distribution on reactant transport and current density distribution. Simulation results reveal that liquid water transport processes and distributions are significantly affected by inlet air velocity, wall wettability and water inlet position, which in turn play a prominent role on local reactant transport and cause considerable disturbances of the current density. Liquid water film spreading on the gas channel (GC) top wall is identified as the most desirable flow pattern in the GC based on overall evaluations of current density magnitude, uniformity of current density distribution and pressure drop in the GC. Modification to GDL structure is proposed to promote the formation of the desirable flow pattern.

Copyright © 2012, Hydrogen Energy Publications, LLC. Published by Elsevier Ltd. All rights reserved.

1. Introduction

Water management in proton exchange membrane fuel cell (PEMFC), especially in the cathode side, is crucial to the cell performance. Successful water management requires deep understanding of liquid water hydrodynamics in gas channel (GC) and porous materials such as gas diffusion layer (GDL) and catalyst layer (CL). Liquid water transport process in GC is of great importance as GC acts as the first step to distribute reactant to the reactive site and the last step to drain the liquid water out of PEMFC [1]. It is affected by various operating conditions such as air flow rate [2], inlet humidity [3], operating temperature [4], and operating load [5]. In addition, it is also affected by several geometrical parameters including

layouts of GC [6], cross sections of GC [7], the channel number and the land/channel width ratio [8] and GC surface wettability [9].

Numerical simulation has been demonstrated as an effective tool to study the above factors affecting liquid water behaviors in GC. Multiphase mixture model [10,11] and multi-fluid multi-phase model [12–14] have been widely adopted in modeling two-phase flow problems in PEMFC. Recently, volume of fluid (VOF) method has also been applied to explore liquid water behaviors in PEMFC, due to its capacity of considering surface tension and wall adhesion and of tracking liquid–gas interface [15–32]. Table 1 presents a partial list of those numerical studies using VOF, which can be divided into different categories based on different classification ways. For

* Corresponding author. Tel./fax: +86 029 82669106.

E-mail address: wqtao@mail.xjtu.edu.cn (W.-Q. Tao).

Table 1 – Simulations of liquid water transport dynamics in the GC using VOF method.

Authors and published year	Components and GC dimensions 3D: height × width × length (mm) 2D: height × length (mm)	Research aspects
Quan et al. [15] 2005	A U-shaped GC 1 × 1 × 20 Smooth GC bottom surface Without water inlet pore	Transport process of liquid water with different initial distribution
Zhan et al. [18] 2006	Single rectangle GC 1 × 1 × 11.5 Single serpentine GC 1 × 1 × 23 Smooth GC bottom surface Without water inlet pore	Effects of air inlet velocity and GC wall wettability on liquid water behaviors
Cai et al. [17] 2006	Single rectangle GC 1 × 1 × 20 GC Bottom surface : smooth Without water inlet pore	Effects of GC wall wettability on liquid water transport and distribution
Theodorakakos et al. [23] 2006	A small fraction of GC Smooth GC bottom surface With water inlet pore	Effects of air velocity on the droplet detachment
Jiao et al. [16] 2006	three parallel GCs 1 × 1 × 10 Smooth GC bottom surface Without water inlet pore	Transport process of liquid water with different initial distribution
Jiao et al. [19] 2006	Serpentine rectangle GCs 1 × 1 × 10 Smooth GC bottom surface Without water inlet pore	Transport process of liquid water with different initial distribution
Jiao et al. [29] 2007	U-shaped GCs with innovative GDL 1 × 1 × 30	Effects of innovative GDL structures on liquid water transport and distribution
Zhu et al. [24] 2007	Single rectangle GC (2D) 0.25 × 1 Smooth GC bottom surface With water inlet pore	Effects of GC size, inlet pore size and air velocity on liquid water dynamic behaviors
Jiao et al. [30] 2008	A U-shaped GC with innovative GDL 1 × 1 × 30	Effects of GDL wettability on liquid water transport and distribution
Ebrahim and Shila [20] 2008	Single rectangle GC (2D) 0.125 × 1 Without water inlet pore	Effects of gas inlet velocity, the density and viscosity of the gas, and the surface tension coefficient on the droplet deformation
Le and Zhou [31] 2008	The whole PEMFC	3D general model for PEMFC involving coupled process of liquid water distribution and reactant transport
Zhu et al. [25] 2008	Single rectangle GC 0.25 × 0.25 × 1 Smooth GC bottom surface With water inlet pore	Effects of inlet air velocity, GC wall wettability, water inlet velocity and water inlet pore size on liquid water distribution
Le and Zhou [32] 2009	The whole PEMFC	3D general model for PEMFC involving coupled process of liquid water distribution and reactant transport
Zhu et al. [26] 2010	Single GC with different cross-sections Smooth GC bottom surface With water inlet pore	Effects of GC cross-sections on liquid water dynamic behaviors.
He et al. [21] 2010	Single rectangle GC 1.05 × 1.05 × 10 Rough GC bottom surface Without water inlet pore	Effects of GC bottom wall surface roughness on liquid water behaviors.
Le et al. [28] 2010	Serpentine rectangle GCs and homogenous GDL	Liquid water transport behaviors within the GDL and GC.
Ding et al. [27] 2010	Single rectangle GC 0.25 × 0.25 × 1.25 Partially rough GC bottom surface With water inlet pore	Effects of water inlet pore structure, water inlet velocity and GC wall wettability on liquid water distribution.
Akhtar and Kerkhof [22] 2011	Single tapered channel Length: 20 height × width (inlet): 1 × 1 height × width (outlet): 0.5 × 1 Smooth GC bottom surface Without water inlet pore	Effects of wall wettability on liquid water behaviors.

the computational domain, some focused on the GC [15–27], some further considered the cathode of the PEMFC [28–30], and some more comprehensively took the whole PEMFC into account [31,32]. For initial liquid water distribution, some started the simulation with initial given liquid water

distribution [15–22,28,31,32] while others performed the simulation with liquid water gradually entering the GC from GDL pores [23–27,29,30]. For the GC bottom surface consisting of GDL, some simply used smooth bottom surface [15–27] while some tried to involve the GDL surface microstructures

Table 2 – Conditions of the baseline case.

Quantity	Value
Inlet air velocity, u_{in}	5 m s ⁻¹
Inlet mass fraction of oxygen, $Y_{o,in}$	0.23
Inlet mass fraction of nitrogen, $Y_{n,in}$	0.71
Inlet mole fraction rate of water vapor, $Y_{wv,in}$	0.0
Contact angle of GDL, θ_{GDL}	140°
Contact angle of GC, θ_{GC}	60°

[21,27]. For the coupling process of liquid water and reactants transport, some concentrated on the liquid water behaviors [15–30] and some further [31,32] simulated the coupled process of liquid water transport and reactant transfer. Based on the above studies, liquid water transport processes in GC can be summarized as follows: Liquid water forms droplets in GC after permeating the hydrophobic GDL; the droplets appear in preferential areas, rather than uniformly along the GC; the detachment mechanism of a droplet is affected by the air flow rate from the upstream, channel design and channel surface characteristics; after detachment, the droplet moves downstream principally in the form of droplets, films or slugs. On the whole, liquid water transport in the GC is significantly complicated due to its inherently unsteady and nonlinear characteristics.

Effects of liquid water distributions in GC on reactant transport are significant as GC acts as the first step to distribute reactant to the reactive site [33,34]; thus, evaluation of such effects is quite required for achieving high cell performance. Liquid water distribution patterns (or two-phase flow patterns) in GC have been identified as mist flow, droplet flow, film flow (annular flow) and slug flow under different operating conditions and physical parameters [35]. Obviously, these different flow patterns in GC cause different reactant transport processes and thus the current density distributions [36]. However, most of the numerical investigations mentioned above focused on the behaviors of liquid water while the reactant transfer was largely neglected. Specially, the above mentioned simulations using VOF usually decoupled reactant transport and reaction from the two-phase hydrodynamics. Therefore, further studies are required in which two-phase interface is explicitly tracked and liquid water effects on reactant transport are quantitatively investigated. Only very recently, Le and Zhou [31,32] conducted studies in such coupled way and revealed the great effects of the liquid water distribution on mass transfer. However, effects of the various operating conditions on water transport process in GC were not examined in their study. Besides, optimization of the GC or GDL structures to improve water management in PEMFC based on the simulation results, the ultimate goal of numerical studies of liquid water behaviors in PEMFC, is still rare in literature and further work is currently required.

The objective of this paper is to investigate liquid water behaviors in the cathode side of a PEMFC under different air inlet velocities and GC wall wettability and to quantitatively evaluate the effects of liquid water distributions on mass transport and current density distribution. Efforts are also devoted to improve the water management in the cathode

side by modifying structures of the GC and GDL based on the simulation results. The rest of this paper is arranged as follows. In Section 2 the computational domain and the numerical methods are introduced. Then, in Section 3 liquid water behaviors in the GC under different air flow rate, wall wettability and water inlet position are depicted. Effects of liquid water distribution on pressure drop in the GC, reactant transport, current density variation and uniformity of the current density distribution are investigated. Finally, some conclusions are drawn in Section 4.

2. Numerical model development

2.1. Computational domain

The bottom wall of the GC is consisted of GDL which is made of porous materials structured by carbon fibers such as carbon paper and carbon cloth. In a carbon paper GDL, the carbon fibers are disarranged and misaligned, generating microscopically complex structures of GDL with random distributions of pore size, as shown in Fig. 1. Therefore, the GDL surface, or the bottom surface of the GC is very rough. In mini/micro channels, the surface microstructures play an important role on water flow characteristics [37]. In this study, to consider the effects of the microstructures of GDL surface on liquid water dynamics in the GC, a hybrid GDL configuration is designed which consists of two layers as shown in Fig. 2(a). The first layer (hereinafter called as first layer GDL) is homogenous without considering the microscopic porous structure of GDL, in which physical properties such as porosity, permeability and gas diffusivity are uniform. Actually, this layer is similar to the isotropic GDL widely adopted in literature in which simulations are based on the macroscopic continuum models [10–14]. On the contrary, the second layer (hereinafter called as second layer GDL), sandwiched between the first layer GDL and the GC, considers the microstructures of GDL. In this layer, the complex GDL structures are described as solid cubes dispersed in void spaces, as shown in Fig. 2(a). The top surfaces of these solid cubes are the top surface of the

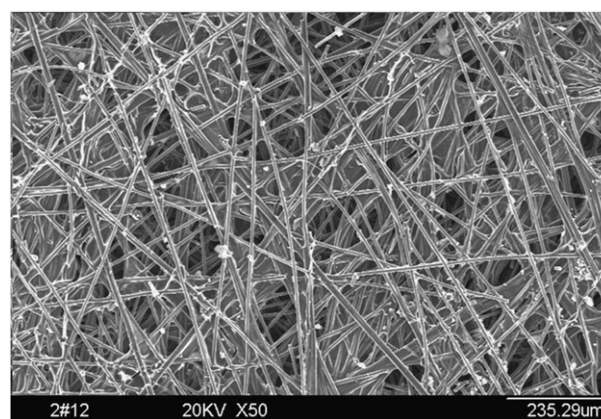


Fig. 1 – Microstructure of carbon paper GDL (TGP 60 with 5% PTFE content, taken by the author's group in Xi'an Jiaotong university, China).

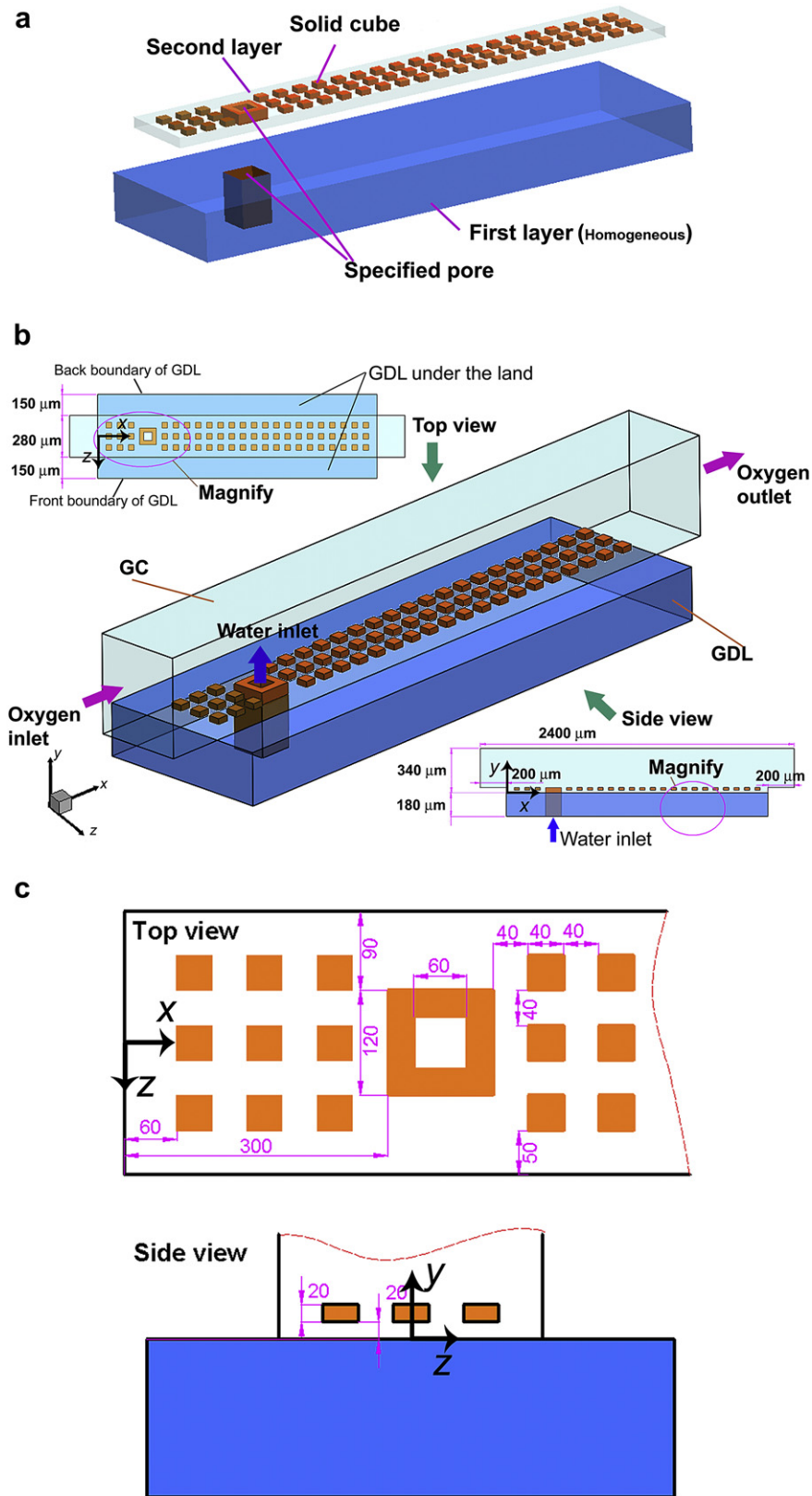


Fig. 2 – Computational domain. (a) hybrid GDL configuration including two layers, (b) Three-dimensional structure, (c) dimensions of the porous second layer GDL.

whole GDL, i.e. the bottom surface of the GC. The structure of the second layer GDL is somewhat simplified compared with the real structure of a carbon paper GDL as shown in Fig. 1. Using such simplified structure is a compromise choice as describing the realistic complex structures of GDL requires huge computational resources [38,39]. In the literature investigating liquid water transport process in GC where surface microstructures of GDL are described, such simplified GDL is commonly used (for example uniformly distributed circular pore structure used in [27] and rectangular rib structure used in [21]) and generally meaningful and helpful results have been obtained [21,27]. On the whole, the hybrid GDL is consciously constructed for two purposes. One is to consider the interaction between liquid water and microstructures of the GDL surface. The other is to save computational resources, since describing the whole GDL as real complex structures requires extremely huge computational resources [38,39].

In an operating PEMFC, liquid water enters the GC from preferential pathway with largest pores within the GDL [2,40]. Within the GDL, the preferential pathway is greatly tortuous [41]. In addition, practically liquid water emerges from GDL at several random locations, and coalescence of liquid water from these random locations usually occurs in the GC [4]. To focus on the dynamics of a single liquid water droplet, the coalescence phenomenon is not considered and the complicated pathway within the GDL is simply regarded as a straight pore completely permeating the GDL in the present study which is similar to Ref. [23,25,26], as shown in Fig. 2(a). Liquid water generated by electrochemical reaction totally invades into the pore and then enters the GC.

The entire computational domain is schematically shown in Fig. 2(b), including a rectangle GC, the hybrid GDL and a CL. The CL is treated as an ultra-thin layer located on the bottom surface of the computational domain, and electrochemical reaction occurs on this surface. The dimensions of the whole computational domain and local dimensions of the GDL are presented in Fig. 2(b) and (c).

2.2. Model assumptions

The general transport process in the domain can be briefly described as follows: air flows into the GC at the left inlet, transports through the second layer GDL, penetrates the first layer GDL and finally arrives at the CL, i.e. the bottom surface of the computational domain. At the bottom surface, electrochemical reaction occurs and oxygen is consumed and water is generated. The generated liquid water invades into the specified pore in the GDL and then enters the GC. In the GC, liquid water grows, deforms and moves towards the GC outlet. The distributions and transport processes of liquid water in turn strongly affect reactant transport and thus the cell performance. In order to numerically explore the basic features of the above complex processes, the following assumptions, which are common in literature [16–18,21,23,25,27,28,30], are made:

1. The gas is ideal gas.
2. The fluid flow is isothermal, unsteady, laminar, and incompressible. It is worth to mention that temperature plays important roles on cell performance. It causes

evaporation or condensation between liquid water and water vapor, affects transport parameters including diffusivity and ion conductivity, and changes the electrochemical reaction rate. In the present work, the phase change between liquid water and water vapor is not considered (see Assumption 3 below), a common assumption in literature using VOF to study two-phase hydrodynamic in GC [16–18,21,23,25,27,28,30]. Besides, only half PEMFC without PEM is investigated and thus effect of temperature on proton conductivity is eliminated. On the whole, effects of temperature on cell performance are limited and the isothermal assumption is reasonable in the present study.

3. There is no mass transfer between the gas and liquid water, namely evaporation or condensation is neglected. In an real operating PEMFC, evaporation plays an important role for the removal of water in the GC under certain operating conditions. For example, experiment results in Ref. [4] show that liquid water completely evaporated in the GC when raising cell temperature to 60 °C and water is removed out of the GC mainly in the vapor phase. In the present study, emphasis is put on liquid water dynamic behaviors in the GC and thus evaporation is not considered. Neglecting evaporation is a common assumption in literature where focus was on liquid water transport processes [16–18,21,23,25,27,28,30].

2.3. Governing equations

In this study, for solving fluid flow and species transport the physical models include the following three conservation principles: mass, momentum and species concentration. In addition, a volume fraction equation based on VOF method is used to track the gas–liquid interface. For completeness, only a brief introduction to these governing equations is given in the following paragraphs. For more details one can refer to Refs. [31,32].

The continuity equation and momentum equation are:

$$\frac{\partial(\rho)}{\partial t} + \nabla \cdot (\rho \mathbf{u}) = 0 \quad (1)$$

$$\frac{\partial(\rho \mathbf{u})}{\partial t} + \nabla \cdot (\rho \mathbf{u} \mathbf{u}) = -\nabla p + \nabla \cdot [\mu (\nabla \mathbf{u} + \nabla \mathbf{u}^T)] + \rho \mathbf{g} + \mathbf{F} \quad (2)$$

where p is the pressure. ρ and μ are volume averaged density and dynamic viscosity, respectively, which are calculated with linear interpolation using the volume fraction function of liquid and gas s_l and s_g

$$\rho = s_l \rho_l + s_g \rho_g \quad (3)$$

$$\mu = s_l \mu_l + s_g \mu_g \quad (4)$$

Note that the sum of s_l and s_g is unity in a computational cell.

\mathbf{F} in Eq. (2) is a momentum source term related to forces except the gravity force. In the GC and the second layer GDL, surface tension force is considered by adopting the continuum surface force (CSF) model [42] and \mathbf{F} is expressed as

$$\mathbf{F} = 2\sigma k \frac{\rho \nabla s_1}{(\rho_l + \rho_g)} \quad (5)$$

where σ is the surface tension coefficient and k is the mean curvature of the liquid/gas interface which is computed from the local gradient of surface normal \mathbf{n} at the interface

$$k = \nabla \cdot \left(\frac{\mathbf{n}}{|\mathbf{n}|} \right) \quad (6)$$

where \mathbf{n} is defined as the gradient of s_1

$$\mathbf{n} = \nabla s_1 \quad (7)$$

In the first layer GDL, the Darcy drag force is also added into the momentum source term, thus \mathbf{F} is calculated by

$$\mathbf{F} = 2\sigma k \frac{\rho \nabla s_1}{(\rho_l + \rho_g)} - \frac{\mu}{k_p} \mathbf{u} \quad (8)$$

where k_p is permeability of the first GDL layer.

In this study, the inlet air is dry with inlet mass fraction of water vapor of zero and the water generated is assumed to be liquid water, thus water vapor transport is absent in the simulation. Only the oxygen transport equation is solved. The species transport equation for oxygen is expressed as follows

$$\frac{\partial(\rho_g Y)}{\partial t} + \nabla \cdot (\rho_g \mathbf{u}_g Y) = -\nabla \cdot (\rho_g D_{\text{eff}} \nabla Y) \quad (9)$$

where Y is the mass fraction of oxygen. D_{eff} is the effective diffusion coefficient and is determined as follows [31]

$$D_{\text{eff}} = [\varepsilon(1 - s_1)]^{1.5} D_0 \quad (10)$$

where ε is the porosity of GDL and D_0 is the binary diffusion coefficient.

VOF is a surface-tracking method that can be used to study the position of interface between two immiscible fluids. The first algorithm of VOF was developed by Hirt and Nichols [43]. In the VOF method, a volume fraction function s_k of k th fluid is defined which is computed in each computational cell. $s_k = 1$ means the computational mesh is full of k th fluid, $0 < s_k < 1$ means the computational cell is partially occupied by k th fluid, and $s_k = 0$ means there is no k th fluid in the computational cell. The sum of s_k in a computational cell is unit. In this study, the tracking of the liquid–gas interface is accomplished by solving the following equation in each computational mesh

$$\frac{\partial(s_1 \rho_1)}{\partial t} + \nabla \cdot (s_1 \rho_1 \mathbf{u}_1) = 0 \quad (11)$$

2.4. Boundary conditions

The following boundary conditions for the computational domain shown in Fig. 2(b) are specified for simulations [25,34]:

(1) At the GC inlet, velocity and species mass fractions are given

$$\begin{aligned} u &= u_{\text{in}}, \quad v = 0, \quad w = 0, \quad Y_o = 0.23, \quad Y_n = 0.77, \\ s_1 &= 0, \quad p = p_{\text{in}} \end{aligned} \quad (12)$$

where the subscripts o and n represent oxygen and nitrogen, respectively. In this work, only a GC with finite length greatly shorter than typical length of a GC in real PEMFC is simulated and the increasingly prominent accumulation of liquid water towards the GC outlet of a PEMFC is not considered. For more details of such accumulation phenomena towards the GC outlet one can refer to [28].

(2) At the GC outlet, out flow boundary condition is adopted

$$\begin{aligned} \partial u / \partial x = 0, \quad \partial v / \partial x = 0, \quad \partial w / \partial x = 0, \quad \partial p / \partial x = 0, \quad \partial Y_o / \partial x = 0, \\ \partial Y_n / \partial x_n = 0, \quad \partial s_1 / \partial x = 0, \end{aligned} \quad (13)$$

(3) At the front ($y \leq 0 \mu\text{m}$ and $z = 290 \mu\text{m}$) and back boundaries ($y \leq 0$ and $z = -290 \mu\text{m}$) of the hybrid GDL, symmetry boundary condition is applied (see Fig. 2(b)).

(4) On all the solid walls in the computational domain

$$u = 0, \quad v = 0, \quad w = 0, \quad \partial Y_o / \partial n = 0, \quad \partial Y_n / \partial n = 0 \quad (14)$$

(5) At liquid water inlet on the bottom surface of the GDL ($y = -180 \mu\text{m}$, $530 \mu\text{m} \leq x \leq 590 \mu\text{m}$, and $-30 \mu\text{m} \leq z \leq 30 \mu\text{m}$, see Fig. 2(b) and (c)) [26]

$$u = 0, \quad v = v_{\text{in}}, \quad w = 0, \quad Y_o = 0, \quad Y_n = 0, \quad s_1 = 1 \quad (15)$$

(6) On the bottom surface (the reactive surface)

$$u = 0, \quad v = 0, \quad w = 0, \quad \partial Y_n / \partial n = 0, \quad D \partial Y_o / \partial n = -\frac{M_o J}{4F}, \quad (16)$$

where M_o is the molecular weight of oxygen and F is the Faraday constant. J is the cathode transfer current density and is calculated by Butler–Volmer correlation relating the local current density to the reactant concentrations [34]

$$J = J_{\text{ref}} \left(\frac{C_o}{C_{o,\text{ref}}} \right)^{r_c} \exp \left(-\frac{\alpha F}{RT} \eta \right) \quad (17)$$

where J_{ref} is the reference exchange current density, α is the transfer coefficient and R is the gas constant. η is the local surface over-potential. r_c is the cathode concentration dependence. During the simulation, constant η is specified on the bottom surface, as given in Table 3. After simulation convergence is achieved, local current density on the CL surface is calculated according to Eq. (17). The average current density is obtained by averaging local current density on the reaction surface.

Values of the parameters required for the boundary conditions described above are listed in Table 2 and Table 3.

2.5. Numerical procedures

In this study, the computational domain is meshed into about 620,000 grid cells for the baseline case by adopting Gambit 2.3 mesh generation software. Then, it is imported into CFD software Fluent 6.3.26 [44] which uses a control-volume-based technique to discrete governing equations into forms that can be solved numerically. In Fluent, pressure-based segregated solver is adopted for an unsteady laminar incompressible flow

Table 3 – Parameters used in the simulation.

Quantity	Value
Porosity of the second layer GDL, ϵ	0.7
Permeability of the second layer GDL, k_p	$1.0 \times 10^{-11} \text{ m}^2$ [10]
Operating temperature, T	333 K
Operating pressure, p	101325 Pa (1 atm)
Universal gas constant, R	$8.314 \text{ J mol}^{-1} \text{ K}^{-1}$
Faraday's constant, F	96487 C mol^{-1}
Surface tension coefficient, σ	0.0725 N m^{-1}
Over-potential specified on the bottom surface, η	0.5 V
Diffusivity of oxygen in air, D_o	$2.84 \times 10^{-5} \text{ m}^2 \text{ s}^{-1}$ [10]
Cathode transfer coefficient, α	0.5 [32]
ORR reduction order, γ_c	1 [10]
Cathode volumetric reference exchange current density/reference oxygen concentration, $A_v j_{ref}/(C_{O,ref})^{\gamma_c}$	120 A mol^{-1} (assumed)

with Green-Gauss cell based gradient evolution. The pressure and velocity are calculated using a body-force-weighted interpolation scheme for computing face pressure and the pressure-implicit with splitting of operators (PISO) scheme for coupling the velocity-pressure. An explicit VOF formulation is adopted to track the interface between the liquid water and air. Second order upwind scheme is used to discretize the convective terms. User defined functions (UDF) are written using C++ for the effective diffusivity in the GDL and boundary conditions of oxygen mass fraction on the bottom surface (reactive surface). For all the simulations in this study, the allowed residual is set as 10^{-6} to ensure the simulation converged. The grid independence is checked by using three different grid systems. The time step is 10^{-7} s, which is set up from the time-step independence examination by using three time steps as 1.5×10^{-7} , 10^{-7} and 8×10^{-8} s.

3. Results and discussion

In this section, liquid water transport processes in the GC under different air velocity and wall wettability are depicted. Then, effects of liquid water distribution on pressure drop in the GC, mass transport and current density distributions are discussed. Table 2 lists the conditions for the baseline case. Table 3 gives values of the parameters used in the model.

3.1. Liquid water transport behaviors

3.1.1. Baseline case

Fig. 3(a) displays the time evolution of liquid water interface in the computational domain for the baseline case. Liquid water emerges from the GDL pore into the GC and gradually forms a droplet with approximately spherical-cap shape due to the dominated surface tension force ($t = 0.017$ s). As the droplet grows bigger, the GC is gradually blocked and air flow becomes increasingly faster. The faster air flow induces stronger shear force and pressure forces exerted on the liquid droplet which

thus elongates downstream. Once the droplet grows bigger enough, the enhanced shear force and pressure force overwhelm the surface tension force and accelerate the bulk of the droplet towards the downstream. Apparently, the droplet accelerated has a higher velocity than the liquid water just emerges from the GDL pore; thus, it detaches from the GDL pore and moves rapidly towards the outlet of the GC ($t = 0.020$ s). During its movement towards the downstream, the detached droplet is lifted by the air around it and touches the GC top wall, being shaped like a nipple ($t = 0.0204$ s). Due to the hydrophilicity of the GC top wall, pressure inside the droplet decreases from the bottom up at this moment. Hence, the detached droplet is entirely sucked to the GC top surface due to this pressure gradient and soon widely spreads as water film on the top wall of the GC ($t = 0.024$ s). The water film formed is then pushed by the air flow and moves downstream the GC. The above liquid water transport process can be briefly described as droplet growth, droplet detachment, droplet lift, droplet attachment to the top wall, and water film spreading on the top wall of GC. Such transport process is the first water transport pattern identified in this study. In the following sections, other patterns will be observed under different inlet air velocities and wall wettability. It is worth mentioning that here and in the later presentation only a cycle of liquid water transport process is depicted, which is enough because liquid water behaviors in the GC exhibit periodic characteristics [5,25]. Here, a cycle is defined as the time from the moment that liquid water emerges from the GC to the moment the detached liquid water is completely drained out of the GC.

It is notable that the lift phenomenon of the detached droplet occurs under relatively smaller GDL contact angle compared with the simulation results in [25] where the GDL surface is smooth. Under the same air and water inlet velocities with the present study, the detached droplet still adheres to the GC bottom surface when GDL contact angle is 140° and the lift phenomenon is observed until the GDL contact angle increases to 180° in [25]. The easier lift of the detached droplet in the present study is because the rough GDL surface adopted in the present study provides less adhesion to the liquid water.

3.1.2. Effects of air velocity

Liquid water behaviors and distributions in the cathode side are greatly affected by air flow rates [2]. In this section, air inlet velocities of 1 and 3 m s^{-1} are selected to investigate the effects of air flow rate on liquid water dynamics. Other boundary conditions are the same as the baseline case.

Fig. 3(b) displays the time evolution of liquid water interface in the computational domain for inlet air velocity as 3 m s^{-1} . Compared with the baseline case, the slow air velocity allows the droplet to grow so big that it touches one of the side walls and quickly spreads on the hydrophilic surface of the side wall ($t = 0.021$ s, $t = 0.0228$ s). Soon after, the spreading film climbs up to the corner between the top wall and the side wall, shaping like a quarter of an egg ($t = 0.024$ s). Then, the film moves along the corner towards GC outlet ($t = 0.036$ s).

Fig. 3(c) shows the time evolution of liquid water interface in the computational domain for inlet air velocity as 1 m s^{-1} . Compared with that in Fig. 3(a) and (b), the droplet grows so bigger that it is attached to both the side walls of the GC due to

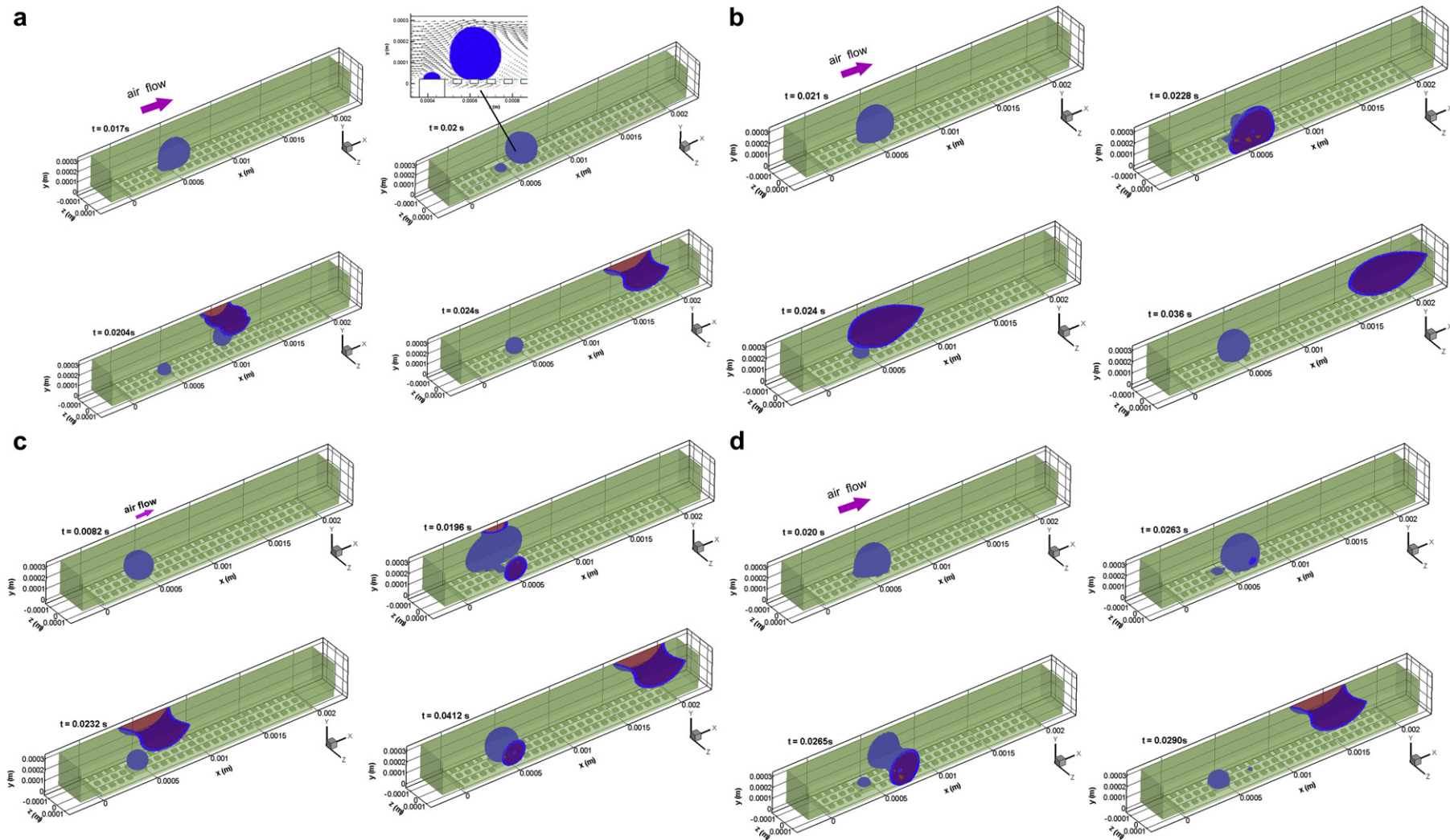


Fig. 3 – Time evolution of liquid water interface in the computational domain. (a) baseline case, air inlet velocity is 5 m s^{-1} , GDL contact angle as 140° , (b) air inlet velocity is 3 m s^{-1} (c) air inlet velocity is 1 m s^{-1} (d) GDL contact angle as 100°

the further reduced air inlet velocity. Owing to the instability of air flow, the bulk of the liquid water mainly spreads on one side wall, leaving a fraction of liquid water on the other side wall ($t = 0.0196$ s). The bulk of the liquid water then mounts up to the corner between the top wall and the side wall, presenting as water film. Compared with Fig. 3(b), the water film is not localized in the corner but further spans across the entire top wall ($t = 0.0232$ s), as surface tension force overwhelms the shear force under the low air flow. The water film across the top wall collects the remaining fraction of liquid water ($t = 0.0232$ s) and moves downstream the GC ($t = 0.0412$ s).

The above liquid water transport processes can be shortly described as droplet growth, droplet attachment to the side walls, droplet detachment from the GDL pore, spreading water film on the top wall or in the corner between the side wall and the top wall. This transport process is the second water transport pattern found in this study. Compared with the baseline case, the droplet attachment occurs before the droplet detachment, due to the lower air velocity which allows the droplet to grow much bigger.

3.1.3. Effects of contact angle

GDL contact angle also plays a significant role on liquid water distributions [24]. Therefore, simulation with GDL contact angle of 100° is performed in this section. Other boundary conditions are the same to the baseline case.

Fig. 3(d) shows the time evolution of liquid water interface in the computational domain for GDL contact angle as 100° . Compared with the baseline case, the droplet detaches with a higher volume due to the lower GDL contact angle ($t = 0.0263$ s) [25]. Immediately after the detachment, the droplet tends to shrink in the flow direction and slightly expands laterally (y and z direction) under the effects of surface tension force; thus it touches the side walls due to its relatively large volume and forms a dumbbell-like shape ($t = 0.0265$). Then, the detached droplet quickly spreads on the side wall, climbs up to the top wall and moves towards the outlet of GC ($t = 0.029$ s).

The above liquid water transport process can be briefly described as droplet growth, droplet detachment, droplet attachment to the side wall, and water film spreading on the top wall. This is the third liquid water transport pattern found in this study. Compared with the baseline case, liquid water is not lifted because the adhesion force between liquid water and the GDL surface increases as contact angle decreases.

Note that in the present study, simulations are also performed for the following three cases: air inlet velocity of 0.1 m s^{-1} , GC contact angle of 40° and GDL contact angle of 120° (In the three cases, other conditions are the same to the baseline case). The simulation results are not presented in detail for simplicity, and only a brief description is given below. For the case with air inlet velocity of 0.1 m s^{-1} , the air flow is not sufficient to sweep the liquid water and the GC is completely blocked, the fourth flow pattern predicted in the present study. For the case with GC contact angle of 40° , the transport process of liquid water is quite similar to the baseline case, with more elongated water film along the flow direction. For case with GDL contact angle of 120° , the detached droplet always slides on the GC bottom wall and is

finally removed out of the GC (For more details of such transport process one can refer to [25]), which is the fifth flow pattern found in the present study. Indeed, liquid water transport processes in GC are various and can be easily changed even one of the various operating conditions and geometrical conditions alters [1]; and this is exactly the cause that arouses extensive studies on liquid water dynamics in GC.

3.2. Effects of liquid water distribution on pressure drop in the GC

Now attention is turned to the effects of liquid water distributions on pressure drop in the GC, mass transport and current density distribution. Pressure drop in the GC is one of the key operating parameters to the cell efficiency. In an unobstructed channel, the pressure drop over a length L should be proportional to the velocity

$$\Delta p = \frac{128\mu A u_{in} L}{\pi D^4} \quad (18)$$

where D is the hydraulic diameter and A is the area of the inlet [45]. Substituting related variables in this study into Eq. (18), the pressure drop calculated is about $18.1u_{in}$ Pa in the GC free of liquid water. Fig. 4(a) shows the time evolution of pressure drop between GC inlet and GC outlet in a cycle under different inlet air velocity, where the time is normalized by the time of a cycle for each case. As can be seen in Fig. 4(a), the pressure drop in the GC free of liquid water at initial time is about 19 Pa, 58 Pa and 101 Pa for inlet air velocity of 1, 3 and 5 m s^{-1} , respectively, agreeing well with the calculated value using Eqs. (18) (18.1, 54.3 and 90.5 Pa for inlet velocity of 1, 3 and 5 m s^{-1} , respectively).

The overall changing trends of the pressure drop under different air inlet velocities are quite similar to each other. Thus, only the variation of the pressure drop for the baseline case is discussed without loss of generality. As time progresses, the pressure drop greatly increases because the GC is gradually blocked by the growing droplet, and undergoes a maximum when the liquid droplet is detached because the GC is most severely blocked at that moment. Then, the pressure drop sharply falls down when the detached droplet spreads as water film. Interestingly, the spreading water film only slightly increases the pressure drop in the GC, compared with that at the initial time when GC is free of water. This is because most of the cross-section of the GC is available for air flow if liquid water spreads on the hydrophilic surface of the top wall. In fact, it has been found that a small decrease of the wall contact angle can create a substantial decrease in the blockage of a channel and thus a great decline in the pressure drop [46].

Note that in Fig. 4(a) that as air inlet velocity decreases, the pressure drop at the end of a cycle is more comparable to the peak pressure drop in this cycle. This implicitly indicates that the next cycle has been developed more adequately at the end of the previous cycle as air inlet velocity decreases.

Fig. 4(b) shows the variation of pressure drop under different GDL contact angles. Before the detached droplet is attached to the top wall, the pressure drop reduces as the GDL contact angle decreases, since smaller GDL contact angle leads to lower droplet in the GC [25]. After the droplet is

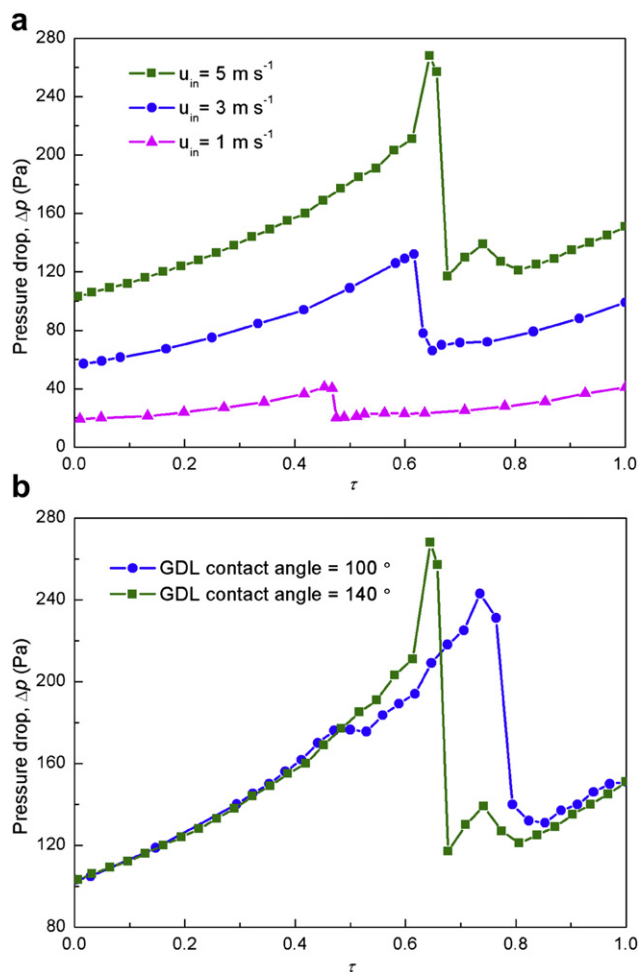


Fig. 4 – Pressure drop between GC inlet and GC outlet in a cycle of liquid water transport. (a) different air inlet velocities, (b) different GDL contact angles.

attached to the top wall, the pressure drop slightly increases as GDL contact angle decreases. This is because the volume of water film spreading on the top wall is larger for lower GDL contact angle, due to the larger detached volume of the water droplet.

3.3. Effects of liquid water distribution on mass transport and current density distribution

The general effects of liquid water distributions in the computational domain on the mass transport and current density distributions under different air velocities and GDL contact angles are quite similar; therefore, in the following the oxygen transport and current density distributions of the baseline case is used for the general discussion.

Liquid water in the GC can significantly affect the oxygen distribution and the corresponding current density distribution. Fig. 5 displays oxygen mole fraction distributions along flow direction (x axis) at some typical times for the baseline case. The contours of the oxygen mass fraction are shown at three slices in z direction. The selected times are very

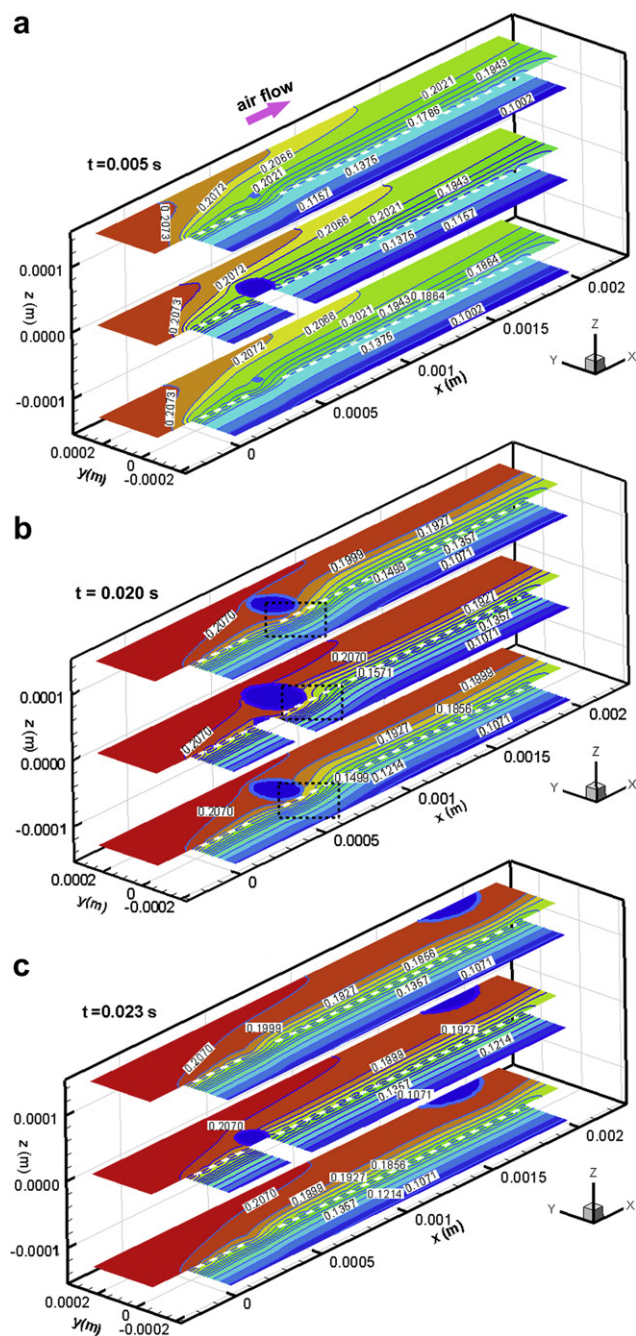


Fig. 5 – Oxygen mole fraction distributions along flow direction (x axis) at some typical times for the baseline case.

representative to discuss effects of liquid water in the GC on reactant transport. It should be mentioned that length ratio between z axis and x axis in Fig. 5 is magnified to provide clearer images. In all the images of Fig. 5, the familiar phenomenon is that the oxygen mole fraction gradually decreases from the GC to the GDL, due to the continual consumption of oxygen by reaction. Fig. 6 presents the corresponding distributions of local current density on the reactive surface (bottom surface of the computational domain). The familiar phenomenon is that local current density

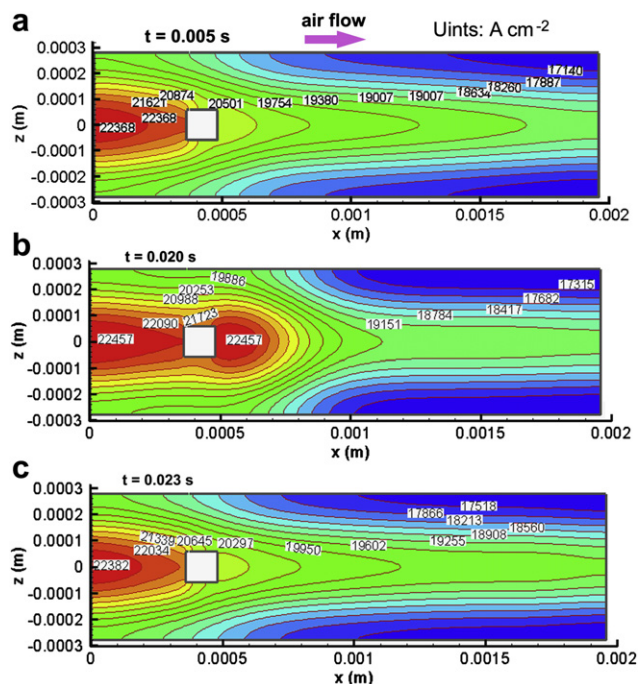


Fig. 6 – Current density distributions on the reactive surface at some typical times for the baseline case.

generally decreases along the flow direction, as the oxygen concentration is gradually reduced. Besides, the local current density in the center of z axis is higher than that in both wings, due to the land shielding effect.

Now attention is turned to the effects of liquid water distribution on local oxygen transport and local current density distribution. At $t = 0.005$ s when the liquid water gradually grows bigger, oxygen is forced to transport in the constricted region between the droplet and the GC (shown in the center slice in Fig. 5(a), $z = 0$ m). In this constricted region, contours of the oxygen mass fraction are greatly elongated to the downstream due to the local stronger air flow. Fig. 6(a) shows the corresponding current density distribution on the reactive surface. The distribution of the current density is greatly affected by the specified pore in the GDL.

At $t = 0.020$ s when the detached droplet is formed, the contours of the oxygen mole fraction under the droplet substantially deflect deep into the GDL (shown in the dashed rectangle in Fig. 5(b)), indicating local enhanced transport of oxygen towards the reactive site. This is because air flow also bypasses into the porous GDL underneath the droplet, thus improving local reactant supply to the reactive site. Obviously, such local improved oxygen supply creates stronger local reaction and thus higher local current density as shown by the peak region in Fig. 6(b). Interestingly, the current density on the entire reactive surface is considerably increased in Fig. 6(b) compared with that in Fig. 6(a), indicating that a detached droplet with appropriate size in the GC provides better cell performance. In fact, in such scenario the detached droplet plays a similar role to a blockage transversely installed in the GC [34]. Perng et al. [34] found that a rectangle in the GC effectively enhances the performance of PEMFC, as the

rectangle positively forces the reactants to permeate deep into the GDL.

At $t = 0.022$ s when the liquid water film moves towards the GC outlet, the contours of the oxygen mole fraction under the water film slightly deflect towards the GDL, as shown in Fig. 5(c), also indicating the local enhanced transport of oxygen towards the reactive site. This is because the water film on the top wall induces an air flow towards the GDL, thus enhancing oxygen transport towards the reactive site and leading to relatively higher current density on the reactive surface under the water film (see Fig. 6(c)), compared with Fig. 6(a) and (b). Actually, the water film on the top wall plays a similar role to the wave structures on the top wall in a wave-like GC [33]. Kuo et al. [33] found that the wave-like structure on the top wall of GC yields a significant increase in the velocity towards the GDL, resulting in increased reactant supply to the reactive site and thus enhanced cell performance. Fig. 7 presents the velocity magnitude around the water film, clearly showing local higher air velocities towards the GDL induced by the water film (in the dashed rectangle).

It should be mentioned that a droplet closely connected to the emergence pore contributes little to force the air flowing into the GDL, because GDL under the emergence pore is filled with liquid water and is not available to reactant transport (see the center slice of Fig. 5(a)). Thus, air mainly flows around the droplet in the GC. As the bulk of the droplet gradually leaves the emergence pore and moves downstream, GDL under the droplet is increasingly available and the enhancement of reactant supply to the reactive site under the droplet can be gradually obtained.

3.4. Variation of the averaged current density and nonuniformity of the current density

Section 3.3 presents a detailed discussion of effects of liquid water distributions on mass transport and current density distribution. In this section, an overall estimation of the liquid water effects on cell performance is provided. Fig. 8(a) illustrates the time evolution of averaged current density on the reactive surface for the baseline case, clearly disclosing that liquid water in the GC causes temporal disturbances of the current density. The averaged current density first decreases at the initial stage when GDL under the droplet is not available to the air flow, then gradually increases when the droplet creeps downstream and the GDL under the droplet is increasingly available, goes through a peak value when the droplet is detached, and then decreases again when the water

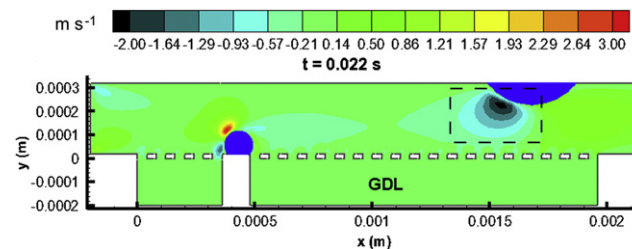


Fig. 7 – Velocity magnitude around the water film on the top wall of the GC.

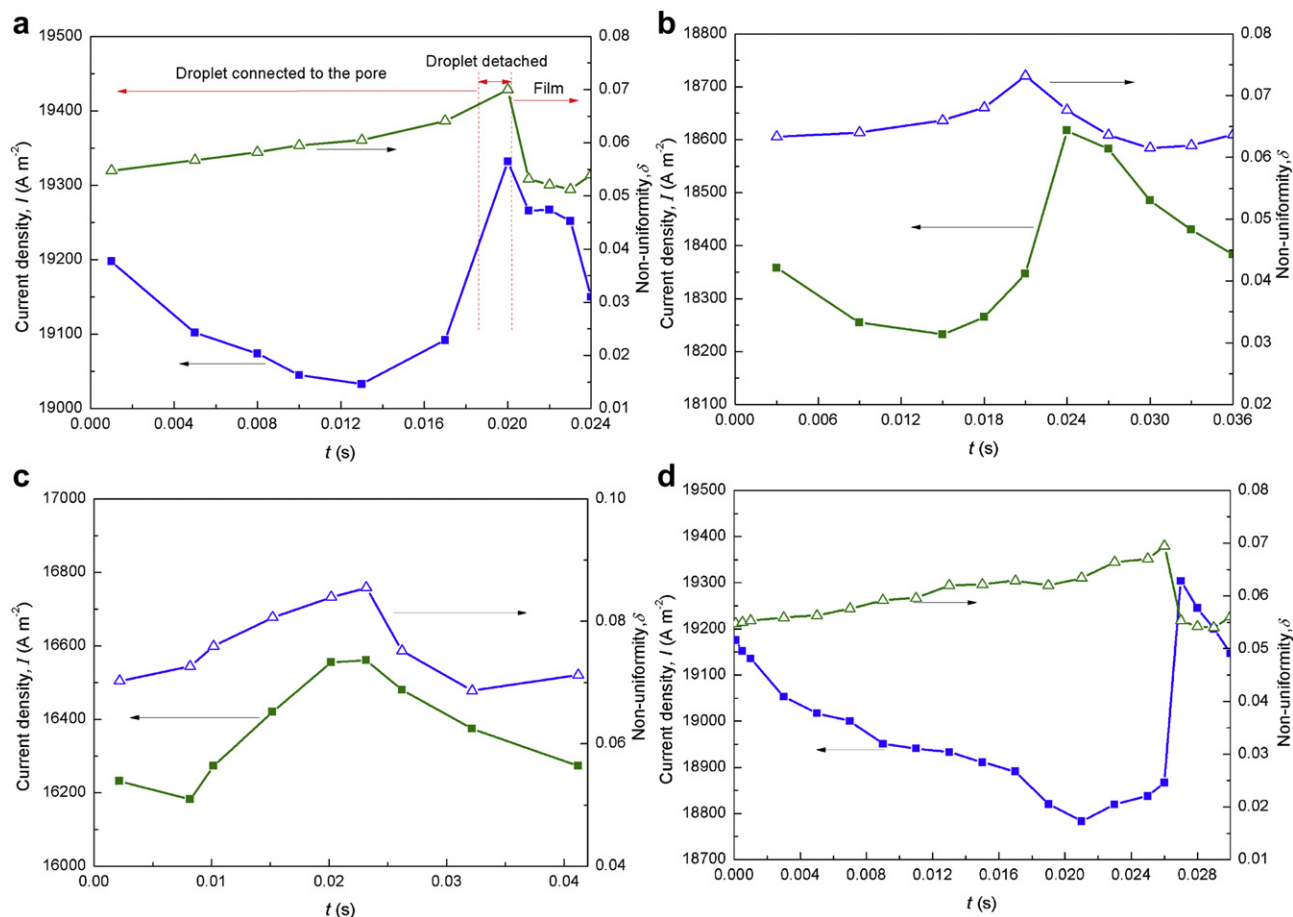


Fig. 8 – Time evolution of averaged current density and nonuniformity of the averaged current density on the reactive surface. (a) baseline case, (b) air inlet velocity is $3 m s^{-1}$ (c) air inlet velocity is $1 m s^{-1}$ (d) GDL contact angle as 100° .

film is formed on the top wall. The change trend of the averaged current density is expected based on the discussion in Section 3.3. Moreover, the detached droplet leads to higher averaged current densities than the water film on the top wall, but this is with the penalty of a higher pressure drop as shown in Fig. 4.

Nonuniform current density distribution in PEMFC can induce local variations in the membrane conductivity, cell temperature and water concentration, causing stresses on the membrane and reducing the lifetime of the cell. Here the nonuniformity of the local current density is evaluated, which is defined as follows

$$\delta = \frac{\sum |I(i, j) - I_{avg}| A(i, j)}{A I_{avg}} \quad (19)$$

where $I(i, j)$ is the local current density, I_{avg} is the average current density. $A(i, j)$ is the area of one computational cell and A is the total area of the reactive surface. The operator $||$ denotes absolute value function. Fig. 8(a) shows the time evolution of nonuniformity of the current density. The detached droplet increases the nonuniformity, because it creates a local peak region as shown in Fig. 6(b). On the contrary, water film creates more uniform current density distribution, even better than the initial time when the GC is free of liquid water, because it ameliorates the reactant supply

downstream the GC and thus leads to more uniformly distributed current density there as shown in Fig. 6(c).

The above simulation results show that the detached droplet in the GC and water film on the GC top wall can enhance the cell performance. Moreover, if liquid water in the PEMFC is unavoidable, the flow pattern of liquid water film on the top wall is more desirable based on an overall evaluation of the magnitude of the current density, uniformity of current density distribution and pressure drop in the GC.

Fig. 8(b) and (c) show the time evolution of averaged current density on the reactive surface and nonuniformity of the local current density for air inlet velocity of 3 and $1 m s^{-1}$, respectively. The averaged current density reduces with decreasing inlet air velocity, which is expected because the slower the air velocity is, the less the oxygen is supplied to the reactive sites. The nonuniformity increases as the inlet air velocity decreases, because lower air inlet velocity provides less oxygen available to reactive surface in the downstream region of the GC. In addition, both the change trends of averaged current density and nonuniformity of current density distribution are similar to the baseline case, further confirming the conclusion that liquid water film on the top wall of GC is the most desirable flow pattern. Fig. 8(d) shows the time evolution of averaged current density on the reactive surface and nonuniformity of the local current density for GDL

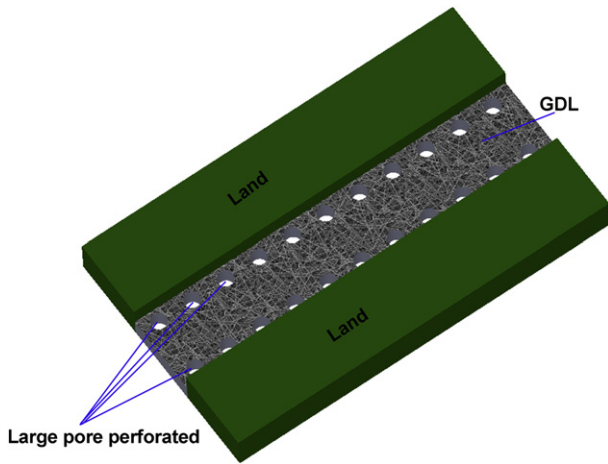


Fig. 9 – Larger pores perforated in the GDL near the side wall of the GC.

contact angle of 100° . The change trend is similar to the baseline case, but the averaged current density is smaller than the baseline case on the whole, because more GDL surface is covered by liquid water under smaller GDL contact angle [25].

3.5. Modification of the GDL structure

Based on the above simulation results, the most desirable flow pattern of liquid water in the GC is water film on the top wall of GC. This is because water film on the top wall creates higher and more uniform current density at the cost of slightly

increased pressure drop in the GC. Note that achieving this desirable flow pattern doesn't require much high air flow rate, and air inlet velocity as low as 1 m s^{-1} is sufficient in this study. In fact, this desirable flow pattern is similar to the annual flow pattern observed in [2], and Trabold also recommended to operate the channels in this flow pattern [47]. While such flow style can be obtained by operating PEMFC under suitable operating conditions, it also can be promoted by modifying GDL geometries. Recently, there have been some researches to artificially perforate larger pores in the GDL to obtain a better water management in the GDL [48]. Liquid water in the GDL preferentially selects these large pores to invade and then enters the GC, leaving other regions within the GDL free of liquid water. Thus, the hysteresis of cell performance is alleviated and the cell performance is substantially improved [48]. Based on the simulation results in the present study, the beneficial effects of these pores can be further enhanced by arranging these pores near the GC side walls (shown in Fig. 9) rather than at the center of the GC in [48], since liquid water can be more easily and quickly wicked to the hydrophilic side walls of GC and effectively forms the desirable flow pattern. Simulations with this suggested pore arrangement in the present study also are performed and the results are presented in Fig. 10. In Fig. 10, liquid water enters the GC ($t = 0.001 \text{ s}$), quickly touches the side wall ($t = 0.002 \text{ s}$) and easily forms the desirable flow style ($t = 0.020 \text{ s}$), compared with the baseline case with the arrangement at the center of the GC as shown in Fig. 3(a). In addition, such pore arrangement is also likely to alleviate flooding within the GDL under the land as liquid water accumulated there can easily migrate into these large pores, leaving large part of the GDL free of liquid water.

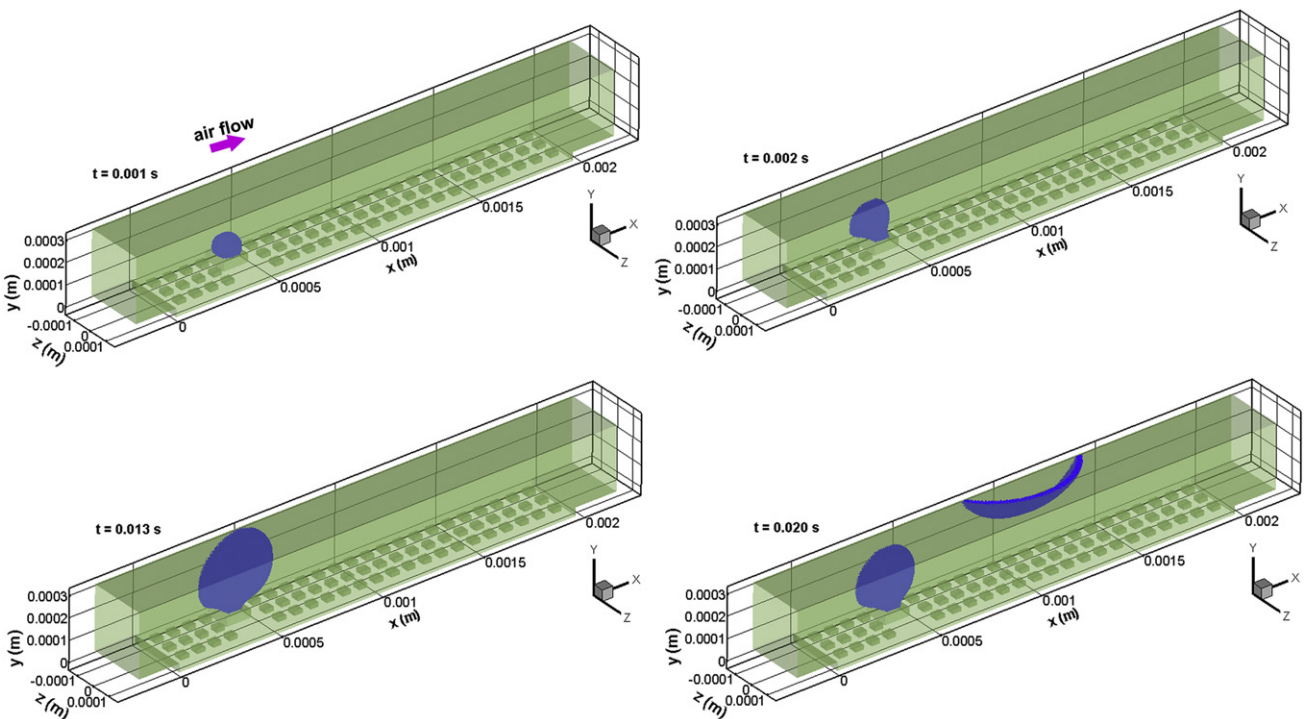


Fig. 10 – Time evolution of liquid water interface in the computational domain for water inlet position near the side wall of the GC.

4. Conclusion

In this study, liquid water behaviors in the GC under different inlet air velocity, wall wettability and water inlet positions are investigated, where a hybrid structural model is adopted to consider the GDL surface microstructures. Effects of liquid water distribution on pressure drop in the GC, reactant transport, current density and uniformity of current density distribution are explored. The main conclusions can be derived as follows:

- (1) Liquid water behaviors and distributions in the GC are quite variable and greatly depend on operating conditions and geometrical conditions. In this study, several kinds of liquid water distributions are numerically identified including water film spanning across the top wall, water film in the corner between the top wall and the side wall, and droplets on the GDL surface.
- (2) The presence of liquid water in the GC increases the pressure drop in the GC. Droplets can severely block the GC and induce high pressure drop. Water film on the top wall only slightly increases the pressure drop in the GC.
- (3) Liquid water distributions in the GC significantly influence the reactant transport and current density distribution. With appropriate size and position, a droplet (liquid water film on the top wall) in the GC generates higher current density. However, the liquid water droplet causes local peak region of current density and leads to high nonuniformity of current density distribution. On the contrary, liquid water film on the top wall can improve the reactant supply downstream the GC and generates more uniform distribution of current density.
- (4) The flow pattern of liquid water film on the top wall of the GC is desirable based on an overall evaluation of the magnitude of the current density, uniformity of current density distribution and pressure drop in the GC.
- (5) Perforating larger pores within the GDL near the side wall of the GC rather than at the center of the GC is helpful to form the desirable flow pattern of liquid water film on the top wall of the GC.

Acknowledgements

The authors thank the National Natural Science Foundation of China (No. 51136004) supporting this work.

Nomenclature

A	Area, m^2
C	Concentration, mol m^{-3}
D	Diffusivity, $m^2 s^{-1}$
D	Hydraulic diameter, m
F	Faraday's constant, $C \text{ mol}^{-1}$
F_{stf}	Surface tension force due to droplet deformation, N
F	Force, N

g	Gravity acceleration, $m s^{-2}$
I	Local current density, $A m^{-2}$
J	Transfer current density, $A m^{-2}$
J_{ref}	Reference exchange current density, $A m^{-2}$
L	Length, m
k	Mean curvature of the interface, m
k_p	Permeability, m^2
M	Molecular weight, $kg \text{ mol}^{-3}$
n, \mathbf{n}	Surface normal
p	Pressure, Pa
R	Universal gas constant, $J \text{ mol}^{-1} K^{-1}$
s	Volume fraction function
t	Time, s
T	Temperature, K
u	Velocity, $m s^{-1}$
U_{in}	Average air inlet velocity, $m s^{-1}$
u, v, w	Velocity, $m s^{-1}$
w	Width of the droplet base, m
Y	Mass fraction
x, y, z	Coordinate

Greek symbols

α	Azimuthal angleCathode transfer coefficient
δ	Nonuniformity
ϵ	Porosity
γ_c	ORR reaction order
η	Over potential, V
μ	Dynamic viscosity, $N s m^{-2}$
σ	Surface tension coefficient, $N m^{-1}$
θ	Contact angle, degree
ρ	Density, $kg m^{-3}$

Subscripts

avg	average
in	Inlet
n	Nitrogen
o	Oxygen
l	Liquid water
g	gas

REFERENCES

- [1] Anderson R, Zhang L, Ding Y, Blanco M, Bi X, Wilkinson DP. A critical review of two-phase flow in gas flow channels of proton exchange membrane fuel cells. *Journal of Power Sources* 2010;195:4531–53.
- [2] Zhang FY, Yang XG, Wang CY. Liquid water removal from a polymer electrolyte fuel cell. *Journal of the Electrochemical Society* 2006;153:A225–32.
- [3] Owejan JP, Trabold TA, Jacobson DL, Baker DR, Hussey DS, Arif M. In situ investigation of water transport in an operating PEM fuel cell using neutron radiography: Part 2-Transient water accumulation in an interdigitated cathode flow field. *International Journal of Heat and Mass Transfer* 2006;49:4721–31.
- [4] Ous T, Arcoumanis C. Visualisation of water accumulation in the flow channels of PEMFC under various operating conditions. *Journal of Power Sources* 2009;187:182–9.
- [5] Pekula N, Heller K, Chuang PA, Turhan A, Mench MM, Brenizer JS, et al. Study of water distribution and transport in a polymer electrolyte fuel cell using neutron imaging.

- Nuclear Instruments and Methods in Physics Research Section A: accelerators, Spectrometers. Detectors and Associated Equipment 2005;542:134–41.
- [6] Spornjak D, Prasad AK, Advani SG. In situ comparison of water content and dynamics in parallel, single-serpentine, and interdigitated flow fields of polymer electrolyte membrane fuel cells. *Journal of Power Sources* 2011;195:3553–68.
- [7] Owejan JP, Trabold TA, Jacobson DL, Arif M, Kandlikar SG. Effects of flow field and diffusion layer properties on water accumulation in a PEM fuel cell. *International Journal of Hydrogen Energy* 2007;32:4489–502.
- [8] Turhan A, Heller K, Brenizer JS, Mench MM. Passive control of liquid water storage and distribution in a PEFC through flow-field design. *Journal of Power Sources* 2008;180:773–83.
- [9] Turhan A, Kim S, Hatzell M, Mench MM. Impact of channel wall hydrophobicity on through-plane water distribution and flooding behavior in a polymer electrolyte fuel cell. *Electrochimica Acta* 2010;55:2734–45.
- [10] Wang ZH, Wang CY, Chen KS. Two-phase flow and transport in the air cathode of proton exchange membrane fuel cells. *Journal of Power Sources* 2001;94:40–50.
- [11] You L, Liu H. A two-phase flow and transport model for the cathode of PEM fuel cells. *International Journal of Heat and Mass Transfer* 2002;45:2277–87.
- [12] Berning T, Djilali N. Three-dimensional computational analysis of transport phenomena in a PEM fuel cell—a parametric study. *Journal of Power Sources* 2003;124:440–52.
- [13] Gurau V, Mann JA, Zawodzinski TA. Two-phase transport in PEM fuel cell cathodes. *Journal of Fuel Cell Science and Technology* 2008;5:021009.
- [14] Gurau V, Mann JA. Effect of interfacial phenomena at the gas diffusion layer-channel interface on the water evolution in a PEMFC. *Journal of the Electrochemical Society* 2010;157: B512–21.
- [15] Quan P, Zhou B, Sobiesiak A, Liu Z. Water behavior in serpentine micro-channel for proton exchange membrane fuel cell cathode. *Journal of Power Sources* 2005;152:131–45.
- [16] Jiao K, Zhou B, Quan P. Liquid water transport in straight micro-parallel-channels with manifolds for PEM fuel cell cathode. *Journal of Power Sources* 2006;157:226–43.
- [17] Cai YH, Hu J, Ma HP, Yi BL, Zhang HM. Effects of hydrophilic/hydrophobic properties on the water behavior in the micro-channels of a proton exchange membrane fuel cell. *Journal of Power Sources* 2006;161:843–8.
- [18] Zhan Z, Xiao J, Pan M, Yuan R. Characteristics of droplet and film water motion in the flow channels of polymer electrolyte membrane fuel cells. *Journal of Power Sources* 2006;160:1–9.
- [19] Jiao K, Zhou B, Quan P. Liquid water transport in parallel serpentine channels with manifolds on cathode side of a PEM fuel cell stack. *Journal of Power Sources* 2006;154:124–37.
- [20] Ebrahim S, Shila M. Deformation of a droplet in a channel flow. *Journal of Fuel Cell Science and Technology* 2008;5: 041008.
- [21] He G, Yamazaki Y, Abudula A. The effect of wall roughness on the liquid removal in micro-channels related to a proton exchange membrane fuel cell (PEMFC). *Journal of Power Sources* 2010;195:1561–8.
- [22] Akhtar N, Kerkhof PJAM. Dynamic behavior of liquid water transport in a tapered channel of a proton exchange membrane fuel cell cathode. *International Journal of Hydrogen Energy* 2011;36:3076–86.
- [23] Theodorakakos A, Ous T, Gavaises M, Nouri JM, Nikolopoulos N, Yanagihara H. Dynamics of water droplets detached from porous surfaces of relevance to PEM fuel cells. *Journal of Colloid and Interface Science* 2006;300:673–87.
- [24] Zhu X, Sui PC, Djilali N. Dynamic behaviour of liquid water emerging from a GDL pore into a PEMFC gas flow channel. *Journal of Power Sources* 2007;172:287–95.
- [25] Zhu X, Sui PC, Djilali N. Three-dimensional numerical simulations of water droplet dynamics in a PEMFC gas channel. *Journal of Power Sources* 2008;181:101–15.
- [26] Zhu X, Liao Q, Sui PC, Djilali N. Numerical investigation of water droplet dynamics in a low-temperature fuel cell microchannel: effect of channel geometry. *Journal of Power Sources* 2010;195:801–12.
- [27] Ding Y, Bi HT, Wilkinson DP. Three-dimensional numerical simulation of water droplet emerging from a gas diffusion layer surface in micro-channels. *Journal of Power Sources* 2010;195:7278–88.
- [28] Le AD, Zhou B, Shiu H-R, Lee C-I, Chang W-C. Numerical simulation and experimental validation of liquid water behaviors in a proton exchange membrane fuel cell cathode with serpentine channels. *Journal of Power Sources* 2010;195: 7302–15.
- [29] Jiao K, Zhou B. Innovative gas diffusion layers and their water removal characteristics in PEM fuel cell cathode. *Journal of Power Sources* 2007;169:296–314.
- [30] Jiao K, Zhou B. Effects of electrode wettabilities on liquid water behaviours in PEM fuel cell cathode. *Journal of Power Sources* 2008;175:106–19.
- [31] Le AD, Zhou B. A general model of proton exchange membrane fuel cell. *Journal of Power Sources* 2008;182: 197–222.
- [32] Le AD, Zhou B. A generalized numerical model for liquid water in a proton exchange membrane fuel cell with interdigitated design. *Journal of Power Sources* 2009;193: 665–83.
- [33] Kuo J-K, Yen T-H, Chen Co-K. Three-dimensional numerical analysis of PEM fuel cells with straight and wave-like gas flow fields channels. *Journal of Power Sources* 2008;177: 96–103.
- [34] Perng S-W, Wu H-W, Jue T-C, Cheng K-C. Numerical predictions of a PEM fuel cell performance enhancement by a rectangular cylinder installed transversely in the flow channel. *Applied Energy* 2009;86:1541–54.
- [35] Lu Z, Kandlikar SG, Rath C, Grimm M, Domigan W, White AD, et al. Water management studies in PEM fuel cells, Part II: Ex situ investigation of flow maldistribution, pressure drop and two-phase flow pattern in gas channels. *International Journal of Hydrogen Energy* 2009;34:3445–56.
- [36] Tüber K, Póca D, Hebling C. Visualization of water buildup in the cathode of a transparent PEM fuel cell. *Journal of Power Sources* 2003;124:403–14.
- [37] Mala GM, Li D. Flow characteristics of water in microtubes. *International Journal of Heat and Fluid Flow* 1999;20: 142–8.
- [38] Park J, Li X. Multi-phase micro-scale flow simulation in the electrodes of a PEM fuel cell by lattice Boltzmann method. *Journal of Power Sources* 2008;178:248–57.
- [39] Mukherjee PP, Wang CY, Kang Q. Mesoscopic modeling of two-phase behavior and flooding phenomena in polymer electrolyte fuel cells. *Electrochimica Acta* 2009; 54:6861–75.
- [40] Litster S, Sinton D, Djilali N. Ex situ visualization of liquid water transport in PEM fuel cell gas diffusion layers. *Journal of Power Sources* 2006;154:95–105.
- [41] Bazylak A, Sinton D, Djilali N. Dynamic water transport and droplet emergence in PEMFC gas diffusion layers. *Journal of Power Sources* 2008;176:240–6.
- [42] Brackbill JU, Kothe DB, Zemach C. A continuum method for modeling surface tension. *Journal of Computational Physics* 1992;100:335–54.

- [43] Hirt CW, Nichols BD. Volume of fluid (VOF) method for the dynamics of free boundaries. *Journal of Computational Physics* 1981;39:201–25.
- [44] Fluent I. *Fluent 6.3 User's Guide* 2006.
- [45] Bird R, Stewart W, Lightfoot E. *Transport phenomena*. 7th ed. New York: Inc: John Wiley & Sons; 1966.
- [46] Venkatraman M, Shimpalee S, Van Zee JW, Moon SI, Extrand CW. Estimates of pressure gradients in PEMFC gas channels due to blockage by static liquid drops. *International Journal of Hydrogen Energy* 2009;34:5522–8.
- [47] Trabold TA. Minichannels in polymer electrolyte membrane fuel cells. *Heat Transfer Engineering* 2005;26:3–12.
- [48] Gerteisen D, Heilmann T, Ziegler C. Enhancing liquid water transport by laser perforation of a GDL in a PEM fuel cell. *Journal of Power Sources* 2008;177:348–54.